ACS Catalysis
Research Article
pubs.acs.org/acscatalysis

Higher Alcohols through CO Hydrogenation over CoCu Catalysts: Influence of Precursor Activation

Yizhi Xiang,[†,‡] Roland Barbosa,[†,‡] and Norbert Kruse*,[†,‡]

[†]Chemical Physics of Materials (Catalysis-Tribology), Université Libre de Bruxelles, Campus Plaine, CP 243, 1050 Brussels, Belgium
[‡]Catalysis for Clean Energy and Environment, Voiland School of Chemical Engineering and Bioengineering, Washington State University, P.O. Box 646515, Pullman, Washington 99164-6515, United States

S *Supporting Information*

ABSTRACT: Bimetallic CoCu model catalysts were investigated for the synthesis of higher alcohols using catalytic CO hydrogenation according to the Fischer–Tropsch technology. Emphasis was placed on revealing the influence of the activation conditions. Accordingly, catalyst precursors were activated in argon, hydrogen, syngas (CO/H_2), and CO under atmospheric conditions and at elevated temperatures (370 °C). All catalyst precursors were prepared via oxalate coprecipitation in the absence of a classic support. Alcohol selectivities between 30 and ~40% (up to ~50% for the sum of alcohols and alkenes) were obtained with an Anderson–Schulz–Flory (ASF) chain lengthening probability maximizing the slate up to C_6. Detailed catalysis and characterization studies were performed using a Co_2Cu_1 catalyst composition. The catalytic performances of the H_2- and syngas-activated Co_2Cu_1 catalyst were similar. While the CO-activated catalyst shows significantly higher catalytic activity and ASF chain lengthening probability, the alcohol selectivities are lower than those of H_2- or syngas-activated ones. All catalysts required time on stream for several hours to achieve steady-state catalytic performance. Co_2Cu_1 catalysts were characterized by temperature-programmed decomposition (TPDec), *in situ* N_2 physisorption (Brunauer–Emmett–Teller), transmission electron microscopy (TEM), and *in situ* X-ray photoelectron spectroscopy (XPS). The data indicate major restructuring occurs during activation. An "onion-like" graphitic carbon shell was observed via TEM for the CO-activated Co_2Cu_1 catalyst, which probably originated mainly from the Boudouard reaction ($2CO + [\ ]_{ad} \rightarrow C_{ad} + CO_2$). This interpretation is in accordance with the TPDec profiles and XPS results. The latter also indicates that syngas and CO activation lead to higher than nominal Co/Cu surface ratios. The surface segregation of Co in the presence of CO atmospheres is interpreted on the basis of Co@Cu core–shell structured particles.

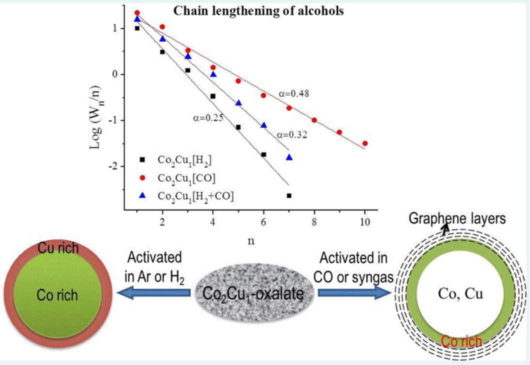

KEYWORDS: *CoCu catalysts, oxalates, thermal decomposition, CO hydrogenation, higher terminal alcohols*

INTRODUCTION

Terminal C_{2+} alcohols play an important role as fuel additives and provide the feedstock for plasticizers, detergents, and lubricants. Traditionally, such alcohols are synthesized through hydroformylation of a C_n ($n \geq 3$) 1-alkene and subsequent hydrogenation of the C_{n+1} aldehydes. Alternative synthetic procedures have been developed more recently as, for example, anti-Markovnikov 1-alkene hydration[1] and one-pot hydroformylation/hydrogenation[2] using homogeneous catalysis. Given the continuing problems in complying with the Markovnikov rule and recovering the noble metals from the homogeneous process, direct CO hydrogenation according to the heterogeneous Fischer–Tropsch (FT) technology may be considered a viable and promising alternative for the future.[3]

The possibility of changing the selectivity of the FT synthesis from hydrocarbons to alcohols consists of replacing Co-based catalysts by bimetallic Co–Cu-based ones. First attempts with the latter were reported by the Institut Francais du Petrole (IFP) in the late 1970s.[4] The focus at that time was on the selective production of C_2–C_6 *iso*- and *n*-alcohols as fuel additives using CO/CO_2-H_2 feeds in an operating manner similar to the industrial methanol synthesis. Most of the present-day studies with such catalysts are aimed at further improving the performance of short chain alcohol synthesis.[4,5]

More recently, it was demonstrated that Co–Cu bimetallic catalysts can be tuned for the selective formation of long chain C_8–C_{14} terminal alcohols using ternary Co–Cu–Mn and Co–Cu–Mo catalysts.[6] Co–Cu–Mn catalysts, prepared by oxalate coprecipitation of the three metals, were shown to exhibit core@shell structured metal nanoparticles, with Co forming the core and all three elements being present in an otherwise Cu-dominated shell with a thickness of ~2 nm.[6] Moreover, metal oxide particles were identified, with Mn_5O_8 forming the most significant oxidic phase. In this work, we focus on binary "CoCu" systems for which phase-separated single metal oxides are much less abundant or even absent. Similar to ternary

Received: May 21, 2014
Revised: July 11, 2014
Published: July 14, 2014

"CoCuMn", binary CoCu powders exhibit a Co@Cu core−shell structure.[6,7] With respect to catalysis, we demonstrate that CoCu, in the absence of a classical support material, produces terminal alcohols with a chain lengthening probability lower than that of "CoCuMn" or "CoCuMo". The combined alcohol/olefin selectivity for certain formulations of these ternary catalysts exceeded the 90% level and demonstrated remarkable long-term performance. The purpose of this paper is to investigate the influence of the activation procedure on the catalytic performance, because core@shell structured CoCu catalyst particles are thought to undergo chemical and structural changes depending on the chemical environment during activation. Major restructuring along with graphitic carbon overlayer formation and Co surface segregation will be demonstrated when a Co_2Cu_1 catalyst is activated in the presence of CO. This way the catalyst activity increases; however, a shift of the selectivities to favor paraffin rather than alcohol formation with otherwise increased ASF chain lengthening behavior is observed. Detailed characterization results from temperature-programmed decomposition (TPDec) studies under various environmental conditions of the oxalic Co_2Cu_1 catalyst precursor will be presented along with results of TEM (transmission electron microscopy) and XPS (X-ray photoelectron spectroscopy).

■ EXPERIMENTAL SECTION

Catalyst Preparation. The oxalate route of catalyst preparation was developed over the past few years in our laboratory and successfully used for binary and ternary metal systems in the absence of a classical support. As for bimetallic Co−Cu, it is well-known from thermodynamics that bulk alloys do not exist. Both metals show low solubility (phase diagrams show a maximum of 9 atom %) with respect to each other. The reason for choosing the oxalate route is associated with the occurrence of polymeric oxalate structures[8] with both metals being chelated in the proximity by oxalate ligands. To produce active catalysts from such a mixed-metal precursor, the oxalate ligand has to be thermally stripped off, which may lead to either CO_2 or CO:

$$MeC_2O_4 \rightarrow Me + 2CO_2 \quad (1)$$

$$MeC_2O_4 \rightarrow MeO + CO + CO_2 \quad (2)$$

The decomposition may be conducted in the presence of either an inert gas (Ar, for example) or hydrogen and/or CO. Under reducing atmospheres, a pure metallic phase may eventually be achieved depending on the nature of the metal (in ternary CoCuMn, for example, a complete reduction of Mn oxides to metallic states is impossible).

CoCu catalysts with varying atomic ratios were prepared as described previously.[6,9] Basically, a solution of adjusted amounts of cobalt nitrate [$Co(NO_3)_2 \cdot 6H_2O$, Aldrich, >98%] and copper nitrate [$Cu(NO_3)_2 \cdot 3H_2O$, Aldrich, >98%] was added to an excess of oxalic acid ($H_2C_2O_4 \cdot 2H_2O$, Acros organics, >99%) in acetone at room temperature while the mixture was being stirred vigorously for at least 5 min. After removal of the supernatant acetone, the precipitated metal oxalate was centrifuged and then dried in air at 100 °C. Finally, the sample was ground and sieved to obtain a size fraction of 125−250 μm for characterization and high-pressure catalytic studies.

Catalyst Testing. High-pressure catalytic tests were performed in a fixed-bed plug-flow reactor consisting of a quartz tubule (Φ_{inner} = 7 mm) inserted into a stainless steel housing. Typically, 1.3 g of CoCu oxalate precursor was diluted with 2 g of SiC to achieve isothermal plug-flow conditions, followed by *in situ* thermal decomposition in H_2, syngas (H_2/CO), or CO at 370 °C for 1 h. After the catalyst precursor had decomposed, the reactor was cooled to <100 °C before being fed with syngas with a H_2/CO ratio of 1.5. Flow rates were adjusted to produce a gas hourly space velocity (GHSV) of 7200 mL g_{cat}^{-1} h^{-1}. After the system had been pressurized to 40 bar, the temperatures for the catalytic tests were approached using low heating rates of 1 °C min^{-1}. The CO conversion and product selectivities were measured by online gas chromatography along with both a thermal conductivity detector (TCD) and a quadrupole mass spectrometer (Agilent 7890A GC/5975 MS).

Catalyst Characterization. Temperature-programmed decomposition (TPDec) of the CoCu oxalate precursor in flowing Ar, 10% H_2, 10% CO, and 10% syngas (5% H_2 and 5% CO) (using Ar as a balance for reactive gases) was performed in a U-shaped microreactor (inner volume of ∼5 cm^3). Suitable amounts of the oxalate precursor were mixed with SiC. The reactor was then heated from room temperature to 375 °C using a 3 °C/min ramp rate while it was being exposed to 30 mL min^{-1} inert (Ar) or reductive gas (10% H_2, 10% CO, or 10% syngas) under atmospheric pressure. The outlet gas phase composition was continuously monitored by a quadrupole mass spectrometer (Balzers, QMG 420-5). Activated catalysts were characterized by *in situ* Brunauer−Emmett−Teller (BET) specific surface area measurements in the same reactor. Finally, the sample was passivated by a 1% O_2/Ar mixture for 1 h to allow *ex situ* TEM characterization.

In situ BET measurements were performed using Ar (diluted in He) as a probe gas. The cross section for nonspecific Ar atom adsorption (σ_{Ar} = 19.2 Å) was determined in calibration experiments with N_2 (σ_{N_2} = 16.2 Å) using an Aerosil 200 instrument (Degussa). Details of the methodological approach have been described previously.[10]

XPS Studies. For XPS studies, the oxalates were heated *in situ* to 400 °C under atmospheric pressure at a flow rate of 30 mL min^{-1} of activating gases [H_2, He, CO, and syngas (H_2/CO)]. These experiments were conducted in a high-pressure reactor (base pressure of 1×10^{-9} mbar) attached to the analytical XPS chamber. The UHV system with a base pressure of 5×10^{-11} mbar has been described in detail previously.[11] Samples were first pelletized and attached to a sample holder that could be placed at choice in the reaction chamber or analytical system using a transfer rod and a rotary distribution chamber. Samples were heated resistively after being exposed to reactive gases. At the end of these chemical treatments, the samples were cooled before they were pumped down the reaction chamber and transferred into the analysis chamber for XPS analysis. The X-ray source was operated with an acceleration voltage of 13 kV and an emission current of 10 mA. Nonmonochromatized Mg Kα radiation was used for the analyses. High-resolution scans were made for Co 2p, Cu 2p, C 1s, O 1s, and Cu LMM employing a pass energy of 50 eV with a dwell time of 0.1 s and a step size of 0.05 eV. After subtraction of the Shirley-type background, the core level spectra were decomposed into components with mixed Gaussian−Lorentzian (G/L) lines using a nonlinear least-squares curve-fitting procedure. The C 1s peak at 284.4 eV was used as the reference energy for charge correction.

The morphology and particle size distribution of CoCu catalysts were determined with a Tecnai G2 F30 S-Twin TEM instrument at an operating voltage of 300 kV. Catalyst samples were passivated in oxygen (1% O_2 in Ar) at room temperature after activation.

RESULTS AND DISCUSSION

This paper is organized as follows. We start by providing the results of catalytic performance tests for several CoCu catalysts with varying atomic amounts of metal. Next we turn to the influence of catalyst activation on performance. To provide a basic understanding of the data, various characterization studies were performed. We start this part of the paper by inspecting the temperature-programmed decomposition spectra of the Co_2Cu_1 oxalate precursor in the presence of either pure argon (Ar), hydrogen (10% H_2 with Ar), carbon monoxide (10% CO with Ar), or syngas (5% H_2/5% CO mixture with Ar). Textural details of this catalyst, after activation in either H_2 or CO (followed by passivation), will be discussed on the basis of TEM or high-resolution TEM [(HR)TEM] results. We finish by presenting XPS data to provide insight into the activation-induced chemical changes of the catalyst surface composition before performance tests.

Catalytic Performance. Table 1 shows the results of catalytic tests with a variety of CoCu catalysts, produced by hydrogen-assisted thermal decomposition of the oxalate precursor at 370 °C, in terms of CO conversion, selectivity, and Anderson−Schulz−Flory (ASF) chain lengthening probability. It is seen that the catalytic activity (CO conversion) and chain lengthening probability increase with increasing relative amounts of Co. The selectivities for the formation of alcohols, alkanes, and alkenes remain almost unchanged for catalysts with Co/Cu ratios of 1/2, 1/1, and 2/1, respectively. A further increase in the Co/Cu ratio to 4/1 results in a decrease in alcohol selectivity and correlates with an increase in alkane and alkene selectivity. All catalysts produce alcohols with a selectivity significantly higher than 30%. Thus, while the selectivity pattern in terms of alcohol production is superior to that of a recent report,[12] it is inferior to those of our ternary metal catalysts "CoCuMn" and "CoCuMo".[6] The ASF chain lengthening probability of CoCu continuously increases with increasing amounts of Co but remains within the range of values representative for a chain lengthening up to about C_5. The combined alcohol/alkene selectivity reaches nearly 50%. Note that both alcohols and alkenes appear with terminal functionality; branched isomers are always detected in insignificant amounts. The CO_2 selectivity over all CoCu catalysts is <3 wt %. Increasing the relative amounts of Co results in a further, albeit slight, decrease in the level of of CO_2 production. This is in accordance with the fact that Co is less active than Cu in the water gas shift reaction.

Table 1. Comparison of the Catalytic Performance of Co−Cu Catalysts with Varying Co/Cu Relative Compositions[a]

		selectivity (wt %)					
catalyst	CO conversion (%)	ROH	RH	$R_=$	CO_2	α_{ROH}	α_{HC}
Co_1Cu_2	2.0	36.7	49.3	11.3	2.7	0.28	0.46
Co_1Cu_1	3.2	37.4	49.4	11.3	1.9	0.30	0.47
Co_2Cu_1	5.7	37.9	50.5	10.2	1.4	0.33	0.47
Co_4Cu_1	11.0	30.8	53.2	15.0	1.0	0.37	0.53

[a] Catalytic tests were conducted at 240 °C, 40 bar, and a H_2/CO ratio of 1.5. CoCu catalysts were obtained by decomposition of the oxalate precursor under flowing H_2 at 370 °C.

The influence of the activation conditions on the catalytic performance was studied for the Co_2Cu_1 catalyst because it offers the best compromise between CO conversion and alcohol selectivity or ASF chain lengthening probability. Figure 1 (and Table S1 of the Supporting Information) shows the data of the catalytic performance after activation in H_2, CO, and syngas (2/1 H_2/CO). It is obvious that the Co_2Cu_1 catalyst activated in CO (denoted Co_2Cu_1[CO]) has a CO hydrogenation activity much higher than that activated in H_2 (Co_2Cu_1[H_2]) or syngas (Co_2Cu_1[Syngas]). The CO conversion at steady state is 27.1% for Co_2Cu_1[CO], while it is only 5.7% for Co_2Cu_1[H_2] and 6.7% for Co_2Cu_1[Syngas]. The steady-state selectivity of alcohols is ∼35%, and the sum selectivity of alcohols and alkenes is ∼50% for both Co_2Cu_1[H_2] and Co_2Cu_1[Syngas]. The corresponding selectivities of alkanes and alkenes are ∼50 and ∼15%, respectively. Quite differently for Co_2Cu_1[CO], the steady-state selectivites of alcohols, alkenes, and alkanes are ∼16, ∼16, and ∼65%, respectively. The CO_2 selectivity is below 3% for all three Co_2Cu_1 catalysts within the entire range of times on stream.

Figure 1 also shows that the steady-state activity and selectivity are reached only after time on stream for several hours. This run-in period, in terms of selectivities, seems to be longer for Co_2Cu_1[H_2] (6 h) than for Co_2Cu_1[CO] and Co_2Cu_1[Syngas] (∼2 h each). With regard to activity, somewhat surprisingly, Co_2Cu_1[Syngas] seems to need times for adjusting steady-state behavior longer than those of the other catalysts. It might have been expected, different from the actual observation, that the activation of the catalyst precursor in the presence of syngas at atmospheric pressure leads to induction periods shorter than those in the presence of either H_2 or CO. Instead, the opposite behavior is observed. It must be concluded that major textural and chemical restructuring of the catalyst is occurring during these early times of operation at elevated pressures. While significant chemical changes are associated with the initial transformation of the oxalate precursor into an active catalyst at atmospheric pressures of reactive gases, the high-pressure synthesis causes such further changes for thermodynamic (production of oxygenates is strongly favored by increasing pressures) and kinetic reasons.

The ASF plots of alcohols, hydrocarbons (alkanes and alkenes), and total "carbons" (alkanes, alkenes, and alcohols) at steady state after activation in H_2, syngas, and CO, respectively, are shown in Figure 2. Accordingly, strictly linear ASF distributions are observed for alcohols over the entire C_n range. The chain lengthening probabilities (α) decrease in the order Co_2Cu_1[H_2] < Co_2Cu_1[Syngas] < Co_2Cu_1[CO], reaching values of 0.25, 0.32, and 0.48, respectively. A slightly different behavior is obtained when all carbon-containing product species are summed in C_{total} for each C_n. While a linear ASF behavior is found for Co_2Cu_1[H_2] and Co_2Cu_1[Syngas], with α values of 0.41 and 0.48, respectively, for the entire C_n range, such linearity with an α of 0.68 is found for Co_2Cu_1[CO] only if the C_1 contribution is discarded. In fact, via inspection of the ASF behavior for hydrocarbon formation (including paraffins and olefins), a large positive deviation is seen for methane. On the other hand, the C_2 hydrocarbons (ethane and ethylene) remain below ASF expectations for all three catalyst activation procedures (note

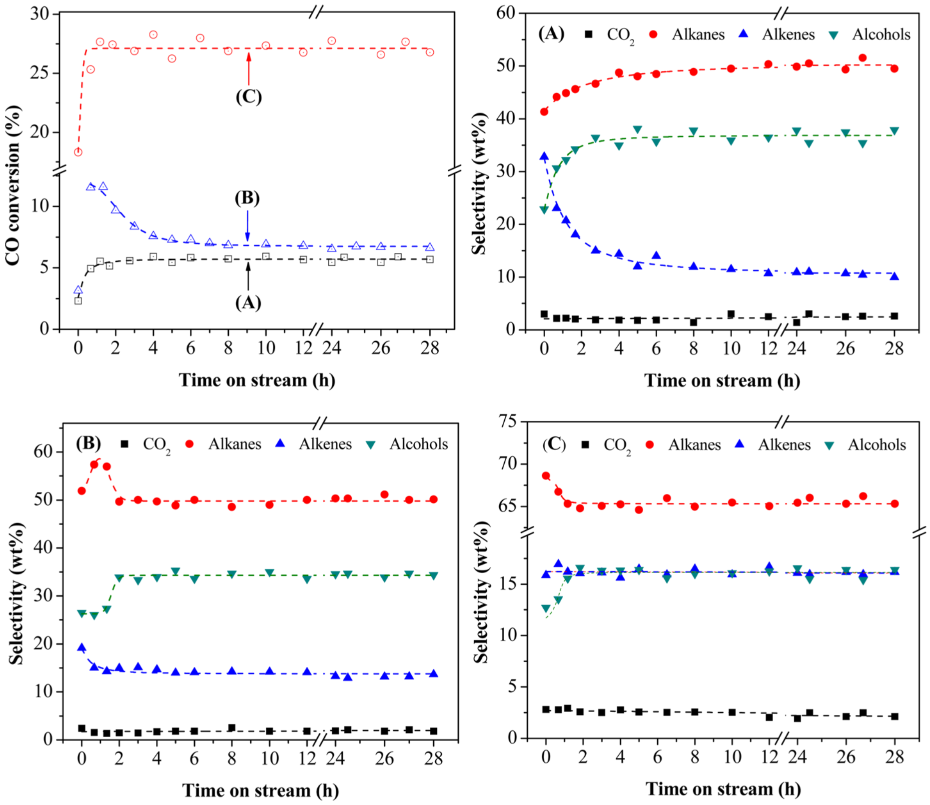

Figure 1. Catalytic performance as a function of time on stream of Co_2Cu_1 catalysts. (A) Decomposition of the oxalate precursor in H_2, (B) syngas (2/1 H_2/CO), and (C) CO. Catalytic tests were conducted at 240 °C, 40 bar, and a H_2/CO ratio of 1.5.

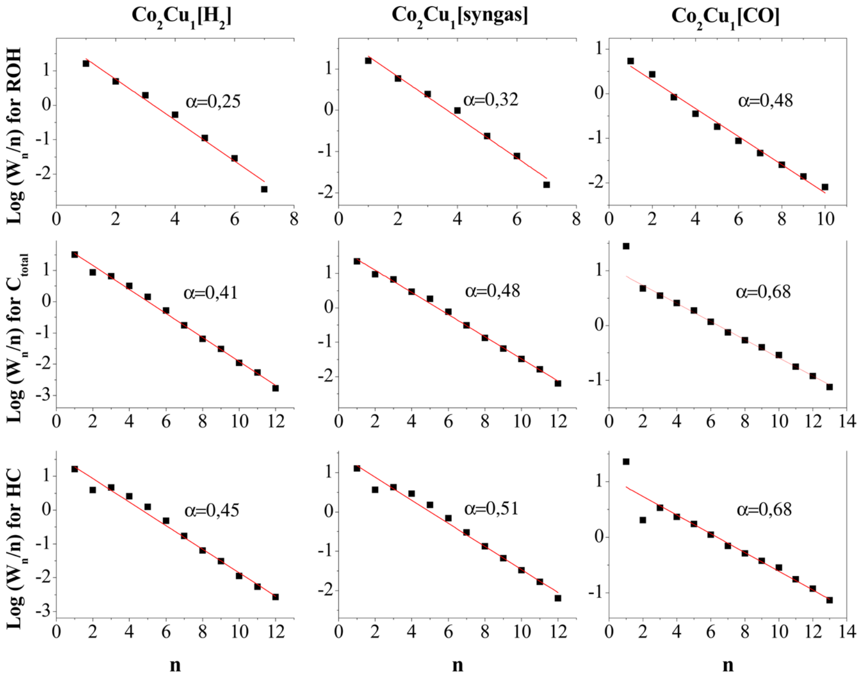

Figure 2. Comparison of ASF plots of alcohols (ROH), total carbon (C_{total}), and hydrocarbons (HC) for Co_2Cu_1 catalysts activated in H_2, syngas, and CO, respectively. $W_n = n(1 - \alpha)^2\alpha^{n-1}$, where W_n stands for the mass fraction of products containing n carbon atoms.

that no significant surplus is seen for C_2H_5OH in ASF plots for alcohols because $\alpha_{ROH} < \alpha_{HC}$). Exceeding methane production is most probably a consequence of massive CO dissociation during the activation process. Excess surface carbon is hydrogenated to methane under high-pressure FT conditions, therefore leading to an "overshoot" for C_1 in the respective ASF plot. The catalytic performance data for the three catalyst activations are also listed in Table S1 of the Supporting Information.

It is clear from the data that activating the Co_2Cu_1 oxalate precursor in CO causes a considerable increase in catalytic activity. This is associated with an increase in the selectivity of

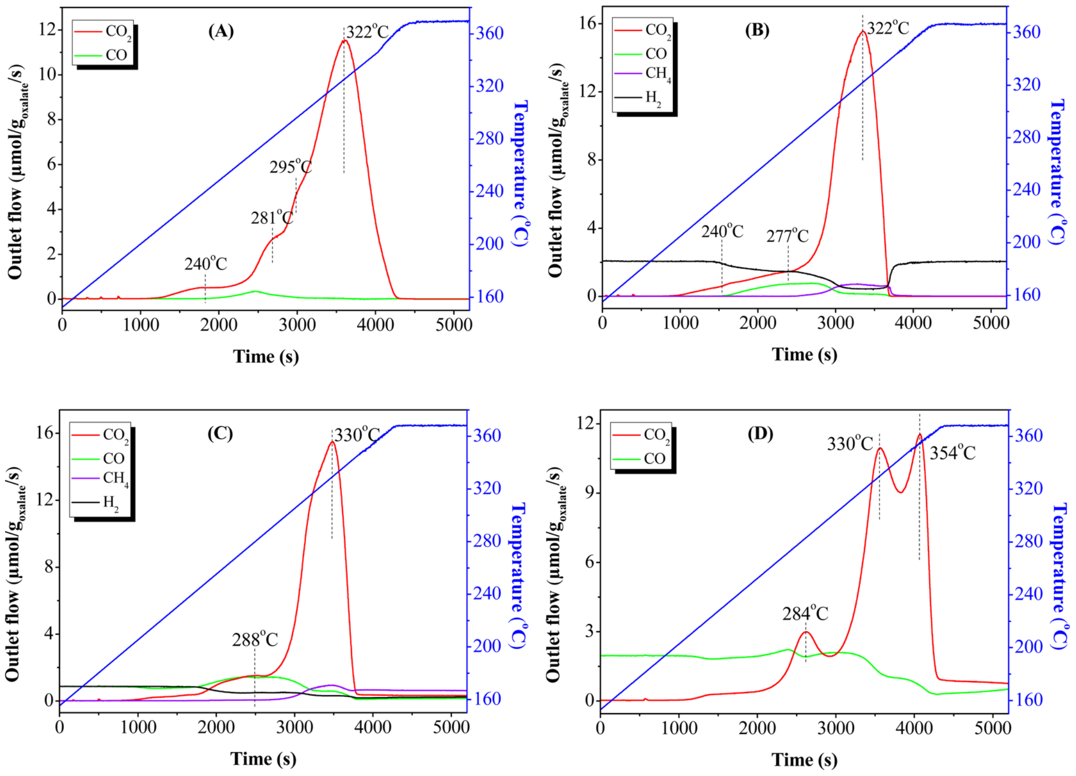

Figure 3. TPDec of the mixed Co_2Cu_1 oxalate in (A) pure Ar, (B) 10% H_2, (C) 10% syngas (5% H_2 and 5% CO), and (D) 10% CO using He as a balance. The temperature was ramped from room temperature to 375 °C at a rate of 3 °C/min followed by isothermal conditions for 1 h. Water is also formed. It is not shown here due to the complicated convolution between the liberation of crystal water from the oxalate precursor and the removal of oxygen formed via decomposition of the oxalate ligand. The quantitative evaluation of the data shows that the sum of carbon-containing molecules (CO_2, CO, and CH_4) desorbing during TPDec is similar for catalysts activated in Ar, H_2, or syngas. Somewhat smaller amounts are obtained in CO-TPDec, possibly because of the formation of surface carbon. The data are compiled in Table S2 of the Supporting Information.

alkane formation. Moreover, the chain lengthening probability for hydrocarbons and alcohols is larger after activation in CO than in any other gas environment. Both $Co_2Cu_1[H_2]$ and Co_2Cu_1[Syngas] show activity lower than that of Co_2Cu_1[CO], yet the alcohol selectivity is much higher for the former. Additionally, both catalysts perform similarly in terms of activity and selectivity, while the chain lengthening probability for Co_2Cu_1[Syngas] seems to be somewhat higher than for $Co_2Cu_1[H_2]$. It is anticipated from these results that the Co/Cu surface ratio is altered during the activation process. An increase in this ratio is expected for the activation in CO. In turn, such "chemical pumping" may lead to significant carbon deposition and, eventually, Co carbide formation, which may significantly alter ASF behaviors for low C_n. Deviations from linear ASF behavior for C_1 due to Co carbide formation have been reported in classical FT work.[13]

Characterization. *Temperature-Programmed Decomposition (TPDec).* Quite generally, the Co and Cu oxalate precursors decompose thermally at temperatures between 200 and 400 °C. According to eqs 1 and 2 of the Experimental Section, either metal or metal oxide is formed depending on whether CO_2, CO, or both are the gaseous products. The extent to which metal oxide forms depends on the chemical environment during the decomposition. Hydrogen-assisted decomposition of the pure oxalates (precipitated in acetone) occurs at 265 °C for Cu and 365 °C for Co.[14]

Figure 3 shows the TPDec spectra (in terms of CO_2, CO, H_2, and CH_4) of the mixed Co_2Cu_1 oxalate precursor in pure Ar, 10% H_2, 10% syngas, and 10% CO. As for Ar-TPDec, one major CO_2 peak at 322 °C, accompanied by two shoulders at ~281 and ~295 °C, and a low-temperature feature at ~240 °C are observed. None of these features coincides with those of the pure Cu or Co oxalate, which is indicative of a CoCu mixed phase oxalate with distinct thermal decomposition behavior. Only a minute amount of CO desorption occurs at ~265 °C, so the CoCu mixed phase precursor mainly decomposes to metallic phases under inert Ar gas. Similar to Ar-TPDec, H_2-TPDec shows a major CO_2 peak temperature at 322 °C.

However, this desorption feature is narrow, and there are no lower-temperature shoulders, as in the Ar-TPDec case. On the other hand, a broad low-temperature CO_2 desorption including the 240 °C feature of the Ar-TPDec experiment is observed. This range of temperatures is partly accompanied by H_2 consumption, which otherwise extends to include the major high-temperature desorption feature, as well. A closer inspection shows hydrogen desorption between 240 and 340 °C to be correlated with CO and CH_4 evolution. The formation of the latter is limited to temperatures between 280 and 340 °C and probably results from partial hydrogenation of CO/CO_2 at metallic patches containing Co.

The spectra of syngas-TPDec are similar to those of H_2-TPDec. The major CO_2 desorption peak now appears at a slightly higher temperature (330 °C), but one still lower than that for pure Co oxalate (365 °C). The profiles of H_2 consumption appear to be correlated with those of CO and methane formation. Note that CH_4 continues to be produced at a constant rate under isothermal conditions once oxalate precursor decomposition is complete. Spectra of CO-TPDec are quite different from those discussed above. Three CO_2 desorption peaks are now observed at 284, 330, and 354 °C. The peak at 330 °C is associated with oxalate decomposition as discussed above. The same applies to the smaller low-temperature feature despite slight variations in the peak temperature as compared to those of H_2-TPDec and syngas-TPDec. The remaining high-temperature feature at 354 °C is new, however. Peak integration shows that this feature roughly adds another 20% to the overall level of CO_2 formation found in H_2- and syngas-TPDec. Furthermore, additional amounts of CO are consumed at higher temperatures and continue to be consumed during the 1 h isothermal conditions following CO-TPDec. We therefore conclude that CO is being irreversibly chemisorbed by decomposition at Co sites of a supposedly Co-rich surface phase. Basically two scenarios have to be considered to explain high-temperature CO_2 formation: CO dissociation and Boudouard reaction ($2CO + [\ ]_{ad} \rightarrow C_{ad} + CO_2$). Because O_{ad} can easily react with CO to form CO_2, both scenarios may contribute to the additionally observed CO_2 production and CO irreversible chemisorption. Further straightforward evidence in favor of this interpretation comes from TP oxidation and H_2-TPR experiments subsequent to CO-TPDec. As shown in Figure S1 of the Supporting Information, surface carbon can be transformed quite easily into CO_2 by TPO while surface carbon can be reacted off as methane (but rather reluctantly, indicating strongly bound states such as those associated with Co carbides).

In summarizing the TPDec results, we find that CoCu mixed oxalates behave differently compared to pure Co and Cu analogues, in agreement with expectations for a common oxalate framework structure of the two metals. The data indicate the formation of Cu-rich and Co-rich phases. Both phases may be associated with core−shell structures. We suggest atom probe tomography (APT) measurements to further characterize such core−shell structures by chemical mapping.

Physical Characterization. After Co_2Cu_1 oxalate precursors had been subjected to TPDec in different chemical environments, the precursors were first characterized by means of BET measurements in the same setup, without displacing the samples. According to Table 2, the BET surface areas (S_{BET}) are 28.5 and 17.5 m^2/g for Co_2Cu_1[Ar] and $Co_2Cu_1[H_2]$ catalysts, respectively. These values are lower than those for Co_2Cu_1[Syngas] and Co_2Cu_1[CO] (~45 m^2/g). Obviously, the presence of CO or CO/H_2 during catalyst activation causes major physical and chemical restructuring. One may suspect from the data that considerable carbon and oxygen deposition occur, possibly leading to surface carbide and oxide formation despite overall reducing conditions. This conclusion is in accordance with "atom counting" results performed while applying chemical transient kinetics to CoCu catalysts. These results demonstrate that carbon and oxygen atoms during the run-in period accumulate in amounts exceeding the monolayer limit.[9,15]

Table 2. *In Situ* Ar Physisorption (BET) of the Co_2Cu_1 Catalysts Activated in Ar, 10% H_2, 10% Syngas, and 10% CO

	Co_2Cu_1[Ar]	$Co_2Cu_1[H_2]$	Co_2Cu_1[Syngas]	Co_2Cu_1[CO]
S_{BET} (m^2/g)	28.5	17.5	43.0	47.5
d (nm)	23.6	38.5	15.7	14.2

Figure 4 shows the results of (HR)TEM characterization of Co_2Cu_1 catalysts after H_2-TPDec and CO-TPDec, followed by passivation through oxygen chemisorption. In general, most of the particles appear to be overlapped in the images, which is expected for metallic catalysts in the absence of a large area support material. Both catalysts show a similar particle size distribution in peripheral areas (where fewer particles overlap) with a size range of 10−25 nm dominating. For Co_2Cu_1[CO], the fraction of >25 nm particles is slightly higher than for $Co_2Cu_1[H_2]$. This is probably due to the formation of an "onion-like" carbon shell embracing Co_2Cu_1[CO] particles. As shown in panels B and C of Figure 4, the shell thickness is around 2−3 nm. The layered structure suggests graphene-type sheets pile up on each other. Such graphitic carbon seems to be rather stable in H_2-TPR for temperatures up to ~500 °C but can be more easily oxidized to CO_2 at ~350 °C during TPO (see Figure S1 of the Supporting Information). Because the FT process involves net reducing conditions, we anticipate the Co_2Cu_1[CO] catalyst retains its graphitic carbon shell during the ongoing CO hydrogenation. A detailed evaluation of lattice structures in Figure 4 is hampered by the occurrence of graphitic overlayers and the similarity of Co and Cu lattice constants. The only particle in Co_2Cu_1[CO] with a lattice spacing of ~0.208 nm can be attributed to the (111) plane of fcc Co or Cu (Figure 4B). One may speculate that small Co clusters with a few atoms are disrupted during activation in CO and placed between the graphene sheets. Such disruptive restructuring cannot be resolved given the limited resolving power of the TEM instrumentation described here. For $Co_2Cu_1[H_2]$ catalysts, fast Fourier transforms of the selected image areas show the existence of hcp Co and fcc Cu or Co. Core−shell structures of Co_2Cu_1 particles do not appear in Figure 4 and would have been difficult to identify given the instrumental limitations.

XPS Surface Analysis. The surface properties of the Co_2Cu_1 catalysts were examined by XPS after *in situ* decomposition under flowing inert gas (He in this case), H_2, syngas, and CO at 400 °C. Spectra for Cu 2p, Co 2p, C 1s, and O 1s are compiled in Figure 5. The Cu 2p profiles for samples heated in H_2, Ar, and syngas are similar but differ somewhat from those obtained upon heating in CO (Figure 5A). Accordingly, while the former demonstrate a metallic Cu^0 state dominates, the latter contains contributions from Cu^0 and Cu^+. Furthermore, all spectra contain small but discernible amounts of Cu^{2+}, as well. More specifically, all samples, whatever the activation procedure, are characterized by a doublet spin split of 19.8 ± 0.1 eV typical of metallic copper. A higher-binding energy shoulder at 935.5 ± 0.06 eV reveals the presence of Cu^{2+} species. Note that the peak at 932.3 ± 0.06 eV is assigned to either Cu^0 or Cu^+. This is because both species have statistically similar BEs, and therefore, the Auger LMM spectra of copper have been used in a qualitative manner to differentiate between the two. These Auger spectra are shown in the Figure S2 of the Supporting Information and demonstrate that all samples, except the one annealed in CO, are mostly in the metallic state. With respect to Co_2Cu_1[CO], besides the larger amounts of Cu^+ compared to the amounts of Cu^0, a negative binding energy shift is observed for Cu^+, with Cu $2p_{3/2}$ and Cu $2p_{1/2}$ binding energies located at 930.7 and 950.6 eV, respectively. This anomalous negative binding energy shift has been attributed to tetrahedral Cu^+ species in cubic spinel oxides.[16] We are not able to challenge this interpretation on the basis of the available data.

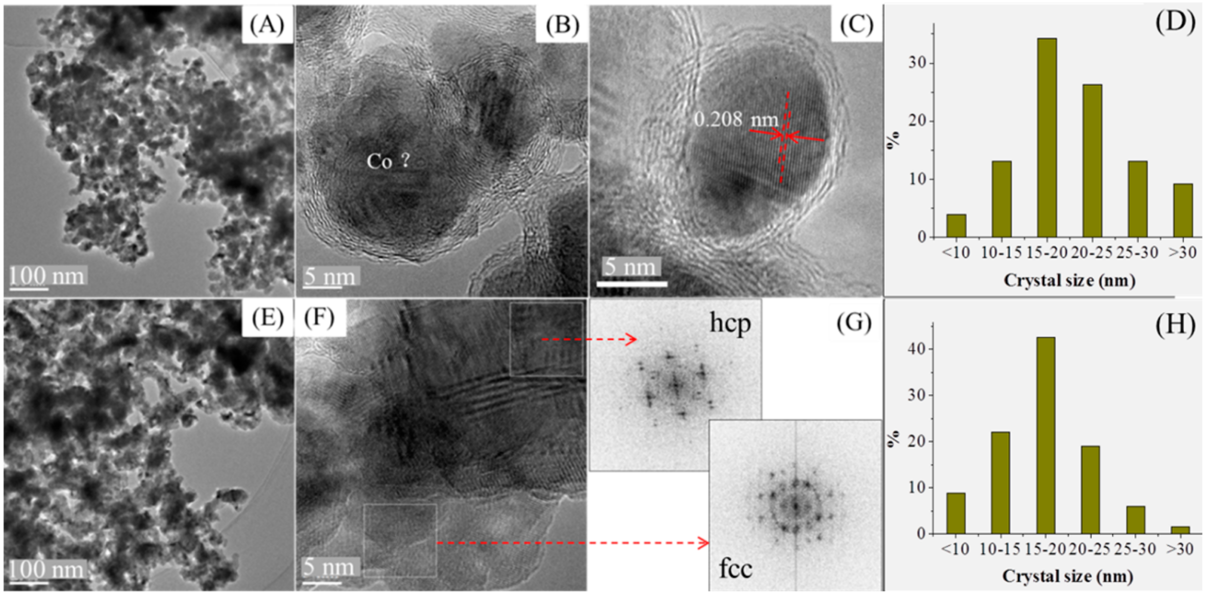

Figure 4. TEM image of Co_2Cu_1 oxalate decomposed in 10% CO (A−C) and 10% H_2 (E and F). (D and H) Particle size distributions for Co_2Cu_1[CO] and $Co_2Cu_1[H_2]$, respectively. (G) Fast Fourier transform of the selected region in panel F.

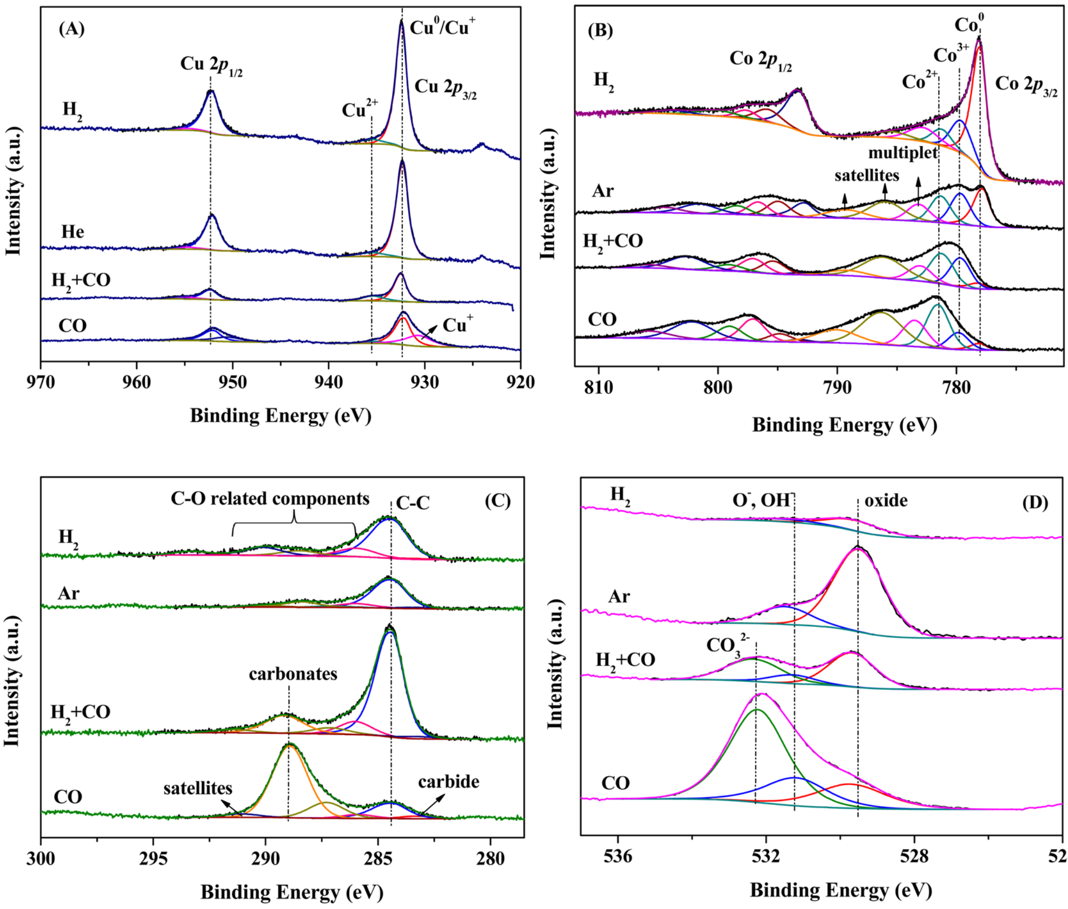

Figure 5. XPS spectra of Co_2Cu_1 catalysts activated *in situ* in He, H_2, syngas, and CO: (A) Cu 2p, (B) Co 2p, (C) C 1s, and (D) O 1s.

Undoubtedly, this result calls for a more extensive spectroscopic investigation.

The presence of both Co^{2+} and Co^{3+} in the corresponding Co 2p spectra confirms the possible presence of a spinel phase (Figure 5B). All of the Co 2p spectra contain Co^0, Co^{2+}, and Co^{3+}; however, the relative intensities vary. Table 3 compiles the relative amounts of cobalt species along with the elemental compositions in the four samples. It is clear, however, that the deconvolution of the Co $2p_{1/2}$ and $2p_{3/2}$ excitations are rather involved because of the occurrence of satellite structures. Regardless, while Co^0 dominates the surface of $Co_2Cu_1[H_2]$, it is the Co^{2+} species that dominates the syngas- and CO-

Table 3. Surface Compositions of the Co_2Cu_1 Oxalates Decomposed in He, H_2, Syngas, and CO from *in Situ* XPS Measurements

activation gas	elemental composition (%) C	O	Co	Cu	Co/Cu ratio	cobalt composition (%) Co^0	Co^{2+}	Co^{3+}
H_2	40.1	8.1	24.0	27.8	0.9	66.7	11.2	22.2
He	23.2	46.5	18.4	11.8	1.6	37.1	29.7	33.2
CO/H_2	54.0	26.4	12.8	6.7	1.9	7.3	50.7	42
CO	30.7	50.1	12.0	7.2	1.7	8.1	68.3	23.5

annealed samples. Thus, while TPDec experiments mainly identify metallic states that form during activation, with the possibility of Co carbide formation in Co_2Cu_1[CO], the surface analysis by XPS demonstrates the existence of higher oxidation states for both metals. Furthermore, the C 1s and O 1s spectra in Figure 5 indicate the presence of carbon and oxygen in amounts varying between "adventitious" (Co_2Cu_1[He] and $Co_2Cu_1[H_2]$) and considerable (Co_2Cu_1[Syngas] and Co_2Cu_1[CO]). In the former case, the exposure to a residual gas atmosphere during *in situ* sample transfer causes C_{ad} and O_{ad} to accumulate before the actual XPS analysis. In the latter case, considerable alterations and specific chemical group formation are observed because of the activation in the presence of syngas or CO. Peaks are assigned to "C—O" species indicating the presence of surface carbonate. It would appear that these species are more abundant after activation in CO. However, only small amounts of carbide and somewhat larger amounts associated with C—C bonds of graphene layers are detected. The apparent disagreement with our TEM results is resolved once the XPS analysis of Co_2Cu_1[CO] is performed after passivating the sample in oxygen. As shown in Figure S3 of the Supporting Information, C—C bonds then dominate the C 1s line profile. We conclude from our combined TEM and XPS results that the graphene-type layered structures are formed during activation in CO and that defects in these sheets are easily saturated by carbonate-type species.

A final observation in relation to our XPS studies addresses the relative surface ratio of Co to Cu (see Table 3). The Co/Cu surface ratio (0.86—1.9/1) is clearly much lower than the bulk nominal ratio (2/1) for all samples. This would be in agreement with the occurrence of a Co@Cu core—shell structure comprising a Co-rich phase in the core and a Cu-dominated shell once the Co_2Cu_1 mixed oxalate has decomposed.[5h,6a,7,12]While the Co/Cu ratio is lowest for activation in H_2, the ratio increases to values of 1.7 and 1.9 for activation in syngas and CO, respectively. Thus, considerable Co segregation takes place under the influence of such chemically reactive environments. The chemical pumping is intensified because Cu-enriched surface phases bind CO relatively weakly. This phenomenon was also observed upon exposure of CuNi catalysts to CO.[17] The interaction of Co with CO gas is much stronger and likely involves the formation of adsorbed subcarbonyls, $Co(CO)_x$ (x = 1—3),[18] in direct competition with CO dissociation or disproportionation. Once the restructuring has been consolidated, Co-rich surface phases can easily decompose CO and accumulate surface carbon, as argued above on the basis of our TPDec, BET, TEM, and XPS results.

CONCLUSIONS

In summary, we showed that bimetallic CoCu catalysts prepared by oxalate coprecipitation are suitable model systems for studying the influence of activation on the production of higher alcohols through catalytic CO hydrogenation. Despite the absence of a classic support material, all catalysts showed stable catalytic performance; however, time on stream for several hours was necessary to achieve the steady state. The catalytic performance of a Co_2Cu_1 formulation was investigated in detail and turned out to be strongly dependent on the gas environment during the thermal decomposition of the mixed metal oxalate precursor. For example, the CO-activated Co_2Cu_1 catalyst showed significantly higher catalytic activity, a higher Anderson—Schulz—Flory chain lengthening probability, but relatively lower alcohol selectivity compared to those of the same catalyst activated in H_2 or syngas. TEM results indicated an "onion-like" graphitic carbon shell on top of the particles. XPS results are in agreement with this observation and indicate the occurrence of C—C bonds once the same activation—passivation procedure was followed as in TEM studies. Furthermore, an evaluation of the XPS Co and Cu 2p intensities demonstrated major Co surface segregation takes place during atmospheric syngas and CO activation.

To put these findings into a more general perspective, we state that the choice of activation conditions is most critical and largely determines the catalytic performance of the catalyst. Major physical and chemical restructuring seems to take place during activation and run-in. This is another clear manifestation of reactant-induced surface segregation and compositional reorganization of surface phases. Similar conclusions were recently reached by Carenco et al.,[19] who reported segregation effects for CuCo@Co nanoparticles prepared to obtain a "CuCo" core and a Co shell (note that the Co@Cu structure as reported in our work is the result of a self-assembly due to the thermal collapse of the mixed metal oxalate network). The authors found Cu enrichment of nanoparticles in the presence of low-pressure syngas while CO was not effective. They explained this finding by assuming a "CO-induced copper enrichment by cobalt extraction" and considered $Co_2(CO)_8$ formation and transport via the gas phase as one of the mechanisms involved in the reconstruction. We mention that this process is thermodynamically not favorable. Instead, similar to what Carenco et al. suggest to be an alternative process, $Co(CO)_x$ surface subcarbonyl formation is the scenario most likely to account for Co atom transport and, therefore, restructuring.[18] There is no doubt that further "operando"-type analytical studies are necessary to reveal the detailed kinetics of surface atom transport under reaction conditions.

In conclusion, while much has been learned about reactant-induced reconstruction in the recent past, little is understood with regard to the underlying mechanisms. These mechanisms form the physicochemical basis of what the chemical engineer calls "know-how" of a catalytic run-in procedure. The Fischer—Tropsch synthesis is an excellent example that demonstrates how the catalytic performance can be controlled by the proper choice of activation conditions as part of spot-on know-how.

■ ASSOCIATED CONTENT

Ⓢ Supporting Information

Tables S1 and S2 and Figures S1−S3. This material is available free of charge via the Internet at http://pubs.acs.org.

■ AUTHOR INFORMATION

Corresponding Author

*E-mail: nkruse@ulb.ac.be or norbert.kruse@wsu.edu.

Notes

The authors declare no competing financial interest.

■ ACKNOWLEDGMENTS

We are grateful for financial support from Total S.A. and thankful for valuable discussions with Daniel Curulla-Ferre (Total S.A.) during this work. Long-term support by the Fonds de la Recherche Scientifique (FNRS) of the Communaute Francaise in Belgium is also gratefully acknowledged. Y.X. gratefully acknowledges the Industrial Catalysis Institute of Zhejiang University of Technology for providing the TEM measurements.

■ REFERENCES

(1) Dong, G.; Teo, P.; Wickens, Z. K.; Grubbs, R. H. *Science* **2011**, *333*, 1609−1612.

(2) (a) Fuchs, D.; Rousseau, G.; Diab, L.; Gellrich, U.; Breit, B. *Angew. Chem., Int. Ed.* **2012**, *51*, 2178−2182. (b) Takahashi, K.; Yamashita, M.; Nozaki, K. *J. Am. Chem. Soc.* **2012**, *134*, 18746−18757.

(3) Forzatti, P.; Tronconi, E.; Pasquon, I. *Catal. Rev.: Sci. Eng.* **1991**, *33*, 109−168.

(4) (a) Courty, P.; Durand, D.; Freund, E.; Sugier, A. *J. Mol. Catal.* **1982**, *17*, 241−254. (b) Xiaoding, X.; Doesburg, E. B. M.; Scholten, J. J. F. *Catal. Today* **1987**, *2*, 125−170.

(5) (a) Baker, J. E.; Burch, R.; Golunski, S. E. *Appl. Catal.* **1989**, *53*, 279−297. (b) Mouaddib, N.; Perrichon, V.; Primet, M. *J. Chem. Soc., Faraday Trans.* **1989**, *85*, 3413−3424. (c) Sheffer, G. R.; Jacobson, R. A.; King, T. S. *J. Catal.* **1989**, *116*, 95−107. (d) Baker, J. E.; Burch, R.; Hibble, S. J.; Loader, P. K. *Appl. Catal.* **1990**, *65*, 281−292. (e) Mouaddib, N.; Perrichon, V.; Martin, G. A. *Appl. Catal., A* **1994**, *118*, 63−72. (f) Subramanian, N. D.; Balaji, G.; Kumar, C. S. S. R.; Spivey, J. J. *Catal. Today* **2009**, *147*, 100−106. (g) Mo, X.; Tsai, Y.-T.; Gao, J.; Mao, D.; Goodwin, J. G., Jr. *J. Catal.* **2012**, *285*, 208−215. (h) Wang, J.; Chernavskii, P. A.; Khodakov, A. Y.; Wang, Y. *J. Catal.* **2012**, *286*, 51−61. (i) Su, J.; Mao, W.; Xu, X.-C.; Yang, Z.; Li, H.; Xu, J.; Han, Y.-F. *AIChE J.* **2014**, *60*, 1797−1809. (j) Prieto, G.; Beijer, S.; Smith, M. L.; He, M.; Au, Y.; Wang, Z.; Bruce, D. A.; de Jong, K. P.; Spivey, J. J.; de Jongh, P. E. *Angew. Chem., Int. Ed.* **2014**, *53*, 6397−6401.

(6) (a) Xiang, Y.; Chitry, V.; Liddicoat, P.; Felfer, P.; Cairney, J.; Ringer, S.; Kruse, N. *J. Am. Chem. Soc.* **2013**, *135*, 7114−7117. (b) Xiang, Y.; Chitry, V.; Kruse, N. *Catal. Lett.* **2013**, *143*, 936−941.

(7) Larde, R.; Bran, J.; Jean, M.; Le Breton, J. M. *Powder Technol.* **2011**, *208*, 260−265.

(8) Donia, A. M.; Dollimore, D. *Thermochim. Acta* **1997**, *290*, 139−147.

(9) Bundhoo, A.; Schweicher, J.; Frennet, A.; Kruse, N. *J. Phys. Chem. C* **2009**, *113*, 10731−10739.

(10) Frennet, A.; Chitry, V.; Kruse, N. *Appl. Catal., A* **2002**, *229*, 273−281.

(11) Chenakin, S. P.; Prada Silvy, R.; Kruse, N. *J. Phys. Chem. B* **2005**, *109*, 14611−14618.

(12) Xiao, K.; Qi, X. Z.; Bao, Z. H.; Wang, X. X.; Zhong, L. S.; Fang, K. G.; Lin, M. G.; Sun, Y. H. *Catal. Sci. Technol.* **2013**, *3*, 1591−1602.

(13) Weller, S.; Hofer, L. J. E.; Anderson, R. B. *J. Am. Chem. Soc.* **1948**, *70*, 799−801.

(14) Barbosa, R.; Xiang, Y.; Kruse, N., manuscript in preparation.

(15) Frennet, A.; Visart de Bocarmé, T.; Bastin, J.-M.; Kruse, N. *J. Phys. Chem. B* **2005**, *109*, 2350−2359.

(16) Kukuruznyak, D. A.; Moyer, J. G.; Prowse, M. S.; Nguyen, N.; Rehr, J. J.; Ohuchi, F. S. *J. Electron Spectrosc. Relat. Phenom.* **2006**, *150*, 282−287.

(17) Studt, F.; Abild-Pedersen, F.; Wu, Q. X.; Jensen, A. D.; Temel, B.; Grunwaldt, J. D.; Norskov, J. K. *J. Catal.* **2012**, *293*, 51−60.

(18) Kruse, N.; Schweicher, J.; Bundhoo, A.; Frennet, A.; de Bocarme, T. V. *Top. Catal.* **2008**, *48*, 145−152.

(19) Carenco, S.; Tuxen, A.; Chintapalli, M.; Pach, E.; Escudero, C.; Ewers, T. D.; Jiang, P.; Borondics, F.; Thornton, G.; Alivisatos, A. P.; Bluhm, H.; Guo, J.; Salmeron, M. *J. Phys. Chem. C* **2013**, *117*, 6259−6266.